Rheology and microstructure of unsaturated wet granular materials: Experiments and simulations

David Hautemayou, Michel Badetti, Abdoulaye Fall, Stéphane Rodts, Patrick Aimedieu, Jean-Noël Roux, François Chevoir

Rheology and microstructure of unsaturated wet granular materials: Experiments and simulations

M. Badetti, A. Fall, D. Hautemayou, F. Chevoir, P. Aimedieu, S. Rodts and J.-N. Roux

Université Paris Est, Laboratoire Navier (UMR 8205 CNRS, IFSTTAR, Ecole des Ponts ParisTech),

2 Allée Kepler, Cité Descartes, F-77420 Champs-sur-Marne

Date: 20/07/18

Abstract

When dealing with unsaturated wet granular materials, a fundamental question is: what is the effect of capillary cohesion on the bulk flow and yield behavior? We investigate the dense-flow rheology of unsaturated granular materials through experiments and discrete element simulations of homogeneous, simple annular shear flows of frictional, cohesive, spherical particles. Dense shear flows of dry, cohesionless granular materials exhibit three regimes: quasistatic, inertial, and intermediate [1]. Herewith, we show that the quasistatic and the intermediate regimes persist for unsaturated materials and that the rheology is essentially described by two dimensionless numbers: the reduced pressure P^* comparing the cohesive to confining forces and the inertial number I, for a wide range of liquid content. This is consistent with recent numerical simulations [2]. Finally, we measure the effective friction coefficient and the solid fraction variation throughout the wet bed. From this we show that, in the quasistatic regime, the Mohr-Coulomb yield criterion is a good approximation for large enough P^*. The experimental results agree quantitatively with the numerical simulations ones provided the intergranular friction coefficient μ is set to its physical value identified from dry material rheology [3]. To directly and quantitatively determine what happens inside the sheared granular bed, X-ray tomography measurements are carried out in a custom-made setup that enables imaging of a wet granular material after different shear histories. For the explored range of liquid content, samples remain homogeneous but exhibit some complex microscopic morphologies far from simple capillary bridges. From the X-ray microtomographic images, we can clearly distinguish liquid capillary bridges and liquid clusters by their morphologies. We see that the total number of capillary bridges decreases when one increases the liquid content and interestingly increases, at the expense of other morphologies, when we increase the shear strain. This explains the concordance between the experimental and numerical measurements since the numerical model is restricted to the *pendular state*, for which the liquid phase is completely discontinuous and no coalescence occurs between liquid bridges.

I. INTRODUCTION

One of the most interesting properties of granular systems is that the grains only interact in the contact points, which form a random network inside the material. However, many powder processing methods such as granulation or coating require humid environments. The presence of liquid affects the properties of granular materials and the behaviour drastically depends on 'how wet' the grains are [4]. Indeed, it is commonly known that the addition of a small amount of liquid in a granular medium creates cohesion properties due to the surface tension of the liquid that wets the grains. Four basic states of wet granular material have been identified [4,5]: *pendular*—liquid bridges between the contact points of the grains; *funicular*—both liquid bridges and liquid-filled pores; *capillary*—almost all the pores filled with liquid; and *slurry*—grains are fully immersed, no capillary action. Generally, these states can be distinguished by the level of liquid content. Such a mixture – unsaturated wet granular materials – may have a strong solidlike behavior [6], and, for instance, enable the building of sand castles as opposed to dry sand which cannot stabilize under gravity with slopes steeper than the angle of repose [7,8].

In the dry case, the rheology is solely dictated by momentum transfer and energy dissipation occurring in direct contacts between grains and with the walls [1]. Despite the simplicity of the system, the behaviour of dry granular materials is very rich and a major step toward describing the rheological properties was the generalization of the Coulomb friction approach [9,10]. This relates the shear stress τ to the confinement pressure σ_n via a friction coefficient μ_d^* that depends on the dimensionless inertial number I (the $\mu(I)-$rheology) [7,9–14].

The presence of a small amount of interstitial fluid in the system introduces another degree of complexity due to the cohesive forces between particles in addition to the friction force in dry granular matter [15]. In the pendular regime, the liquid, in which the pressure is lower than in the void phase, creates adhesive forces. Their macroscopic effects, in the quasistatic regime, are traditionally described in terms of a cohesion, c, appearing in the Mohr-Coulomb condition as:

$$\tau = \mu_d^* \sigma_n + c \qquad \text{(Eq.1)}$$

in which μ_d^* the macroscopic friction coefficient of the dry grain assemblies [16]. The cohesion c vanishes for cohesionless materials such as dry sands. The Mohr-Coulomb stability criterion is analogous to the well-known Coulomb friction law for two sliding surfaces.

The strong influence of the capillary forces on the shear strength is perhaps the most reported property of wet granular materials. However, investigations are mostly limited to the quasistatic behaviours and the influence of shear rate on the mechanical properties is less studied. Bocquet et al. [17,18] studied the effect of waiting time on the repose angle of glass beads contained in a rotating tumbler, and found logarithmic aging of the maximum static angle. They argued that this originates from capillary condensation of water vapor between the packed particles, which results in the formation of liquid bridges.

Wet granular behaviours have been studied in different experimental devices: in a rotating drum [19,20], in a shear apparatus [21], in a segregation flow [22,23] and in a vibrating bed [24]. The system starts to flow when the externally imposed stress exceeds the inter-aggregate contact forces [25]. It was found that a transition from a gaseous regime to a viscoplastic regime occurs when the liquid content reaches a critical point, which is dependent on the particle size [26]. In wet granular systems, liquid bridges are formed by small regions of liquid in the contact area of particles, in which due to surface tension effects a low capillary pressure prevails. Existing studies thus indicate that cohesion strongly affects the behaviour of dense granular flow as well as its microstructure: the mechanical properties at small liquid content are determined by the liquid bridges between grains, and those at larger liquid content are determined by the flow of the liquid through the pores [27]. Besides, the characterization of flow properties is very different; these materials are reported to exhibit a mixed behavior of elasticity, viscosity, and plasticity [19,28]. The reason is that, the few existing studies were done in setups in which shear banding (shear localization) and avalanches strongly influence the apparent rheology, and so it is not obvious that results for a given setup can be translated to a generally applicable conclusion.

In order to attain a general understanding of the role of cohesion in granular materials, it was shown from Discrete Element Method simulations (DEM) that the internal state of the material, in shear flow under controlled normal pressure σ_n [2,29–32], depends on two dimensionless parameters: a reduced pressure P^* (similar to the "cohesion number" which was defined as $\eta = 1/P^*$ in [29,32]) comparing the cohesive to confining forces and an inertial number defined as $I = \dot{\gamma} d_p / \sqrt{\sigma_n / \rho_p}$.

The simplest model of a granular material in the presence of a wetting liquid in small amount assumes the liquid to be confined in menisci at contacts or in narrow gaps between neighbouring grains [33]. The pairwise attractive force that stems from such liquid bridges is well known [5]. It was implemented in DEM simulations [2,34–37], resulting in good agreements with macroscopic experimental results [37–39] of some quasistatic properties. For monodisperse grains, the adhesion force F_0 is the only

internal force and it should be compared to the contact forces induced by the confining stress. Hence, the cohesion of the system is characterized by P^* defined as:

$$P^* = \frac{\sigma_n d_p^2}{F_0} \approx \frac{\sigma_n d_p}{\pi\ \Gamma} \qquad \text{(Eq.2)}$$

where $F_0 = \pi d_p \Gamma$ is the maximum capillary force between a pair of grains (assuming that the contact angle of the liquid with the surface of the beads is small) and Γ the liquid surface tension. When P^* $\gg$ 1, the confining forces are dominant and the effects of cohesive forces are negligible. The case $P^* \to +\infty$ corresponds to cohesionless systems. In the case of $P^* \ll 1$, the effects of cohesive forces become dominant, which may strongly affect the material properties [2]. Thus P^* is a critical microscopic parameter that controls the macroscopic rheology of the system. Thereby P^* extends the rheology of inertial flows to cohesive granular materials [2].

From DEM simulations, it has been thus observed [30,40] that with different cohesive granular models, cohesive forces are expected to have strong effects, possibly enabling very loose equilibrium microstructures for $P^* \ll 1$, while the properties of cohesionless systems are retrieved in the limit of large P^*. Note that results in 2D as well as in 3D simulations, lower P^* values increase the effective friction coefficient $\mu_w^* = \tau / \sigma_n$ and decrease the solid fraction ϕ_S of the wet sheared granular material (unsaturated granular material). However, the effect on μ_w^* is considerably larger in the assembly of wet particles in three dimensions: even for $P^* = 1$ [2,29,31,32]. Although those simulations were restricted to the *pendular* regime (independent menisci) and used simple rules for liquid distribution (e.g., constant meniscus volume), some straightforward extensions are possible, as regards, in particular, the rules governing liquid transport and exchange between different menisci [41–43]. In the same time, viscous effects, which affect the interaction law and might strongly affect the dynamics [44], have not been included into simulations. Nevertheless, they revealed a wealth of remarkable phenomena extending the rheology of dry granular to cohesive granular materials.

At higher liquid content, inter-granular liquid bridges merge, as observed in X-ray microtomography [6,45,46], thereby undermining the adequacy of the binary interaction model as implemented, e. g., in [37], with its simple rules for the spatial distribution of the liquid. It has been found a rich variety of liquid cluster morphologies [33] beyond the well-studied liquid bridge regime. The number and the size of observed liquid clusters strongly depend on the liquid content. Herminghaus [6] showed that the average number of liquid bridges increased with the increasing liquid content, and reached a stable

123 value when the liquid content exceeded a critical value. The self-diffusion coefficient, defined from the
124 mean-square diffusive displacements of grains, and the fluctuation velocities also decrease as the
125 liquid content and liquid viscosity in the wet granular system increase [47,48]. As liquid content
126 increases further, the pores among grains are progressively filled and at some point the system
127 becomes a dense suspension, where both grain-liquid and grain-grain interactions play important roles
128 [5]. The basic physics is that shear strength starts to increase when capillary bridges form between the
129 grains. For increasing liquid fraction, the capillary bridges merge and eventually disappear when the
130 granular media is fully saturated. There must be a maximum strength at a finite amount of added
131 liquid. Indeed, the magnitude of the cohesive forces at different liquid content is intimately linked to
132 the morphology of the interstitial fluids on the scale of single grains [45,49]. Bruchon and co-workers
133 used X-ray Computer Tomography (CT) to analyze changes in the three-dimensional grain skeleton
134 structure upon wetting a sand [50]. In their tests, a small cylindrical specimen of loose sand was wetted
135 from the bottom and simultaneously scanned in a CT-device. The results indicated that the local
136 collapse behaviour is related to the coalescence of capillary bridges in the grain skeleton upon wetting.
137 However, investigations of the influence of cohesion on the flow property of wet granular materials
138 are mostly limited to the quasistatic regime and the influence of shear rate on the mechanical
139 properties in relation to the microstructure does not exist to our knowledge.

140 In this paper, we try to bring new insights on these issues by carefully analyzing the flow of unsaturated
141 wet grains in the dense regime, following the work of [2,29,32] but with an emphasis on the
142 quantitative determination of the microstructure and rheological laws. In order to establish the
143 constitutive laws of the flow of wet granular material, we impose a large enough strain rate to the
144 sample to approach steady flow regime wherein we can measure macroscopic quantities such as shear
145 stress and solid volume fraction for a given confining pressure. Experimental results, in terms of friction
146 coefficient and solid volume fraction variations as functions of the inertial number and the reduced
147 pressure, are then compared to DEM simulations carried out on model wet granular material using the
148 same method as in [2,30]. To obtain the details of the grain packing geometry and the liquid
149 distribution within the sheared sample, we also used a home-made velocity-controlled rheometer
150 coupled to an X-ray microtomograph to characterize the sample' microstructure.

151

152 ## II. MATERIALS AND METHODS

153 ### 1. WET GRANULAR MATERIALS

154 The experiments are carried out on model materials: slightly polydisperse assemblies of macroscopic
155 solid spherical beads, mixed with a non-volatile, wetting, Newtonian liquid. We use rigid polystyrene

beads (Dynoseeds TS 500, Microbeads SA) of density ρ_p = 1050 kg/m^3 and of diameter d_p = 0.5 mm (with a standard deviation of 5%, sufficient to prevent crystallization). We always prepare the system for measurements in the same way to insure reproducible experimental conditions. Subsequently, silicone oil (viscosity 50 mPa.s; density 0.95 g.cm^{-3}; surface tension $\Gamma =$ 20.6 mN/m and wetting angle between 2° and 5°) is mixed thoroughly with the dry beads, after which the system is poured into the shear cell and compacted by repeated tapping. We define the liquid content as $\varepsilon = V_\ell / V_s$, where V_ℓ and V_s are the volumes of liquid and solid beads respectively. Different liquid contents were tested ($\varepsilon \in [0.015 - 0.075]$) corresponding to the *pendular* state [4]. We use silicon oil rather than water since the polystyrene beads are not wettable by water and to avoid evaporative losses. Note that we have checked by NMR (data not shown) that drainage occurs for $\varepsilon > 0.075$: the liquid flows towards the bottom of the sample. All experiments discussed below are carried out, at ambient conditions, by preparing a homogeneous material.

2. X-RAY MICROTOMOGRAPHY

To obtain the details of the grain packing and the liquid morphology within the granular pile, we carried out X-ray microtomography (X-ray CT) experiments. X-ray CT is an imaging tool frequently used in materials science to provide three-dimensional structural information of complex materials in a non-destructive way [33,50].

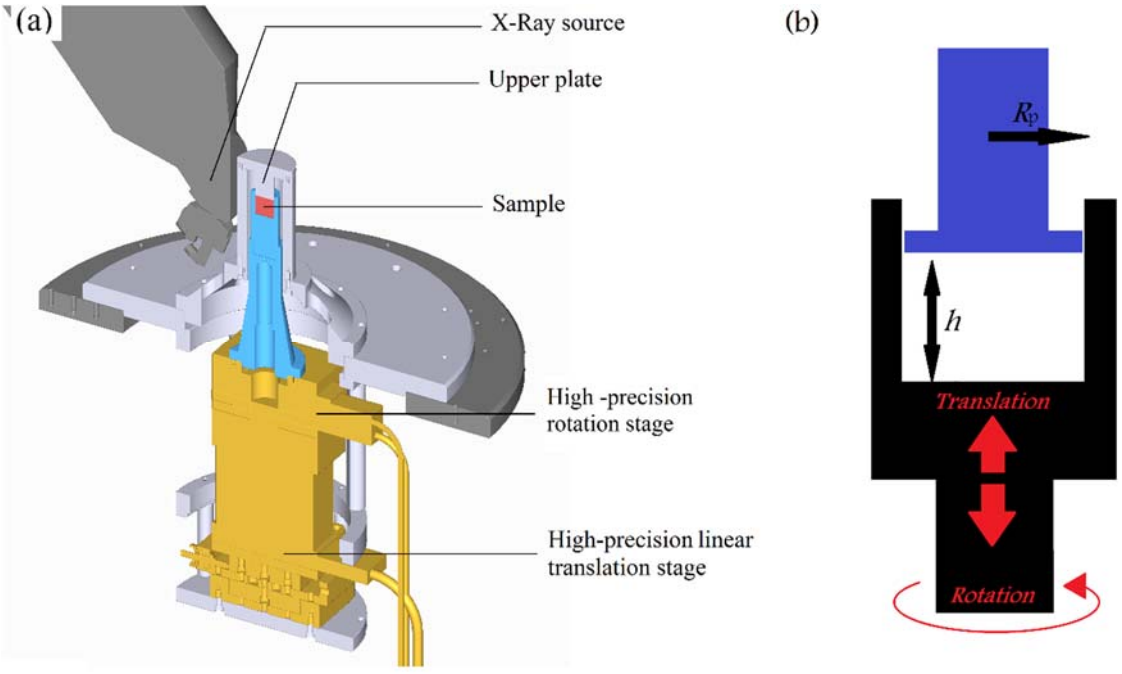

Figure 1: (a) Home-made velocity-controlled rheometer coupled to the X-Ray microtomography. (b) Parallel plate- cup geometry.

176

177 The wet sample is placed into a parallel plate in cup geometry (Fig. 1b) (of $h = 9$ mm of gap and $R_p =$
178 10 mm of radius) in a home-made velocity-controlled rheometer which is inserted into the X-ray
179 microtomograph (Gholami et al. 2017; Deboeuf et al. 2018). Our home-made velocity controlled
180 rheometer consists of two rotary and linear translation motorized stages (Newport, RGV100BL and
181 GTS30V respectively) (Fig. 1a). Both, with a high precision, ensure the implementation of samples and
182 perform the rheological solicitations.

183 The X-Ray microtomography measurements are conducted with an *Ultratom* scanner from *RX*
184 *Solutions*, equipped with a *L10801 Hamamatsu* X-ray source (source parameters: 110 kV–125 µA)
185 associated with a *Varian PaxScan* 2520V flat panel detector used at full resolution. 3D images encoding
186 for the X-ray absorption field are reconstructed from the recorded 2D radiographs. Consistently with
187 the definition of the final 3D images, 1440 projections were taken over 360° rotation with small
188 rotation steps. Note that for each rotation angle, 8 radiographs (with an exposure time for one
189 radiograph of 0.25 s) have been averaged to improve the signal to noise ratio. The final 3D images had
190 a spatial resolution (the voxel size of the image) of 14 µm and a definition of 1648x1294x1678 voxels.
191 Note that, with our X-ray CT device and the chosen spatial resolution, the whole sample can be scanned
192 in 45 minutes. Subsequently, the three-dimensional gray scale images generated by the reconstruction
193 algorithm were processed with *XAct* from *RX Solutions*.

194 ## 3. STEADY SHEAR EXPERIMENTS UNDER CONFINEMENT PRESSURE

195 Steady shear experiments were done using two types of *stress-controlled* rheometers (*Kinexus Pro* by
196 *Malvern* and *MCR 502* by *Anton Paar*) with an annular shear cell geometry (Fig. 2) with, respectively,
197 inner and outer radii of $R_i =$ 21mm and $R_o =$ 45mm [11]. The width of the annular trough is about
198 $48\,d_p$ leading to a ratio of inner to outer wall radii of 0.46. To avoid wall slip, both the moving upper
199 boundary and the static lower boundary are serrated, with 0.5mm ridges that correspond to the size
200 of grains.

201 The normal stress-controlled annular apparatus was designed to carry out such experiments, in which
202 the granular phase may dilate or contract, depending on the density necessary to support σ_n under
203 the imposed strain rate $\dot{\gamma}$. Instead of setting the value of the gap size for a given experiment, as in
204 previous studies [54] and generally in rheometric measurements, we impose the normal force (i.e., the
205 confining normal stress σ_n) and then, under shear, we let the gap size vary in order to maintain the

desired value of the normal force. We then have access to instantaneous measurements of the driving torque T and the gap h variation for imposed normal force F_n and $\dot{\gamma}$: in this case, the solid volume fraction ϕ_S is not fixed but adjusts to the imposed shear [11,55,56]. For our experimental system: surface tension of silicon oil, Γ= 20.6 mN/m, particle diameter d_p = 0.5 mm and at a normal stress σ_n =129.4 Pa, one gets P^* = 1.

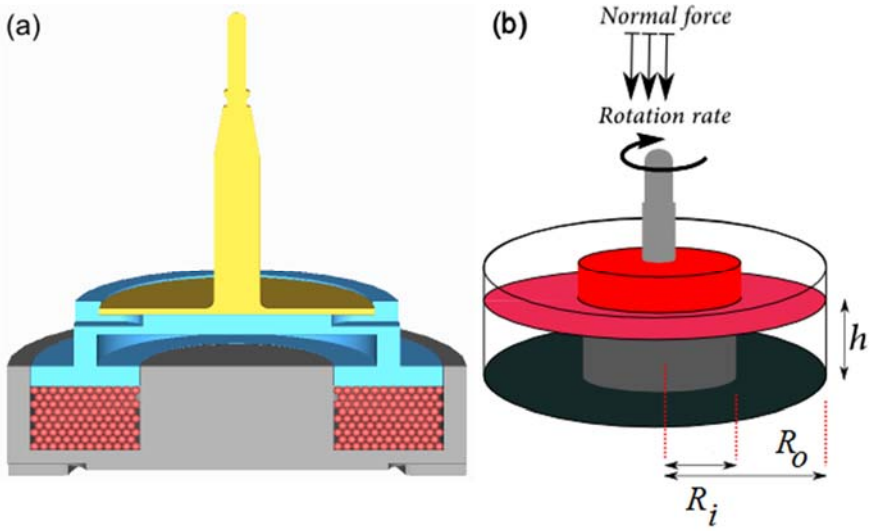

Figure 2: (a) and (b) Cross section of the annular plane shear flow. The shear and pressure are provided by a ring which is assembled on the rheometer that is free to move vertically while maintaining a constant rotation rate or shear rate and imposed pressure.

4. NUMERICAL SIMULATIONS

DEM simulations were carried out on model wet granular materials. The simulated systems are assemblies of monodisperse spherical beads of diameter d_p, interacting in their contacts by Hertz-Mindlin elastic-frictional forces [2,3,30]. Let us stress however, that the intergranular friction coefficient is fixed to $\mu = 0.09$ in order to capture the experimental data of polystyrene dry grains [3]. Indeed in the quasistatic regime, numerical simulations show that both μ_d^* and ϕ_S of dry grains are functions of μ: while the solid fraction is a decreasing function, the internal friction coefficient increases with increasing μ as previously reported [57]. For wet granular materials, we assume that the value of μ does not change in the presence of the wetting liquid [55] and we fix the meniscus volume V_0, as a parameter of the numerical model, in the pendular regime in which the liquid forms disjoint menisci bridging pairs of grains in contact or close to one another. Menisci form when the

grains come into contact. However, if the grains subsequently move apart from each other, the meniscus deforms and breaks when the distance between their surfaces reaches the rupture threshold $D_0 \sim V_0^{1/3}$ as observed in [58–60].

For small volumes, liquid bridges introduce attractive capillary forces for which the Maugis model [61] is adopted for simulations as in [2,30] and the maximum force for contacting particles is given by $F_0 = \pi d_p \Gamma$. The capillary force varies with the distance h between particle surfaces as:

$$F_{cap} = \begin{cases} -F_0, & h \le 0 \\ -F_0 \left(1 - \dfrac{1}{\sqrt{1 + \dfrac{2V_0}{\pi d_p h^2}}} \right), & 0 < h \le D_0 \\ 0, & h > D_0 \end{cases} \qquad \text{(Eq.3)}$$

The liquid content is defined as $\varepsilon = \dfrac{3ZV_0}{\pi d_p^3}$ where Z is the liquid bridge network coordination number (average number of bridges connecting one grain to its neighbours).

For the simulations, 4000 spherical beads are placed in a cubic shear cell, periodic in all three dimensions with an adjustable height. The Lees-Edwards method [2] is implemented to impose the shear rate under a constant normal stress. From time series measurements of the stress components and solid fraction, shear stress and solid fraction are then measured and averaged in the steady state flow (see [2,3] for more details).

III. RESULTS

1. IMAGE ANALYSIS AND LIQUID MORPHOLOGIES

Due to the different X-ray absorption contrast of the three phases: liquid, beads and air, each one can be clearly distinguished from each other. Horizontal slices through 3D tomographic images are shown in Fig. 3 for liquid contents of $\varepsilon = 0.015$, $\varepsilon = 0.03$, and $\varepsilon = 0.075$ respectively.

At $\varepsilon = 0.015$ only capillary bridges can be found in the sample exclusively at the contacts of grains. Above a critical liquid content $0.015 < \varepsilon < 0.03$, intergranular liquid bridges merge in clusters. Whereas for a larger liquid content $\varepsilon = 0.03$, liquid clusters are visible; liquid bridges around the contact points and liquid-filled pores coexist. For an even larger liquid content $\varepsilon = 0.075$, more pores

are filled with the liquid. The liquid surface forms large pockets within the material and larger clusters between many beads have formed [62].

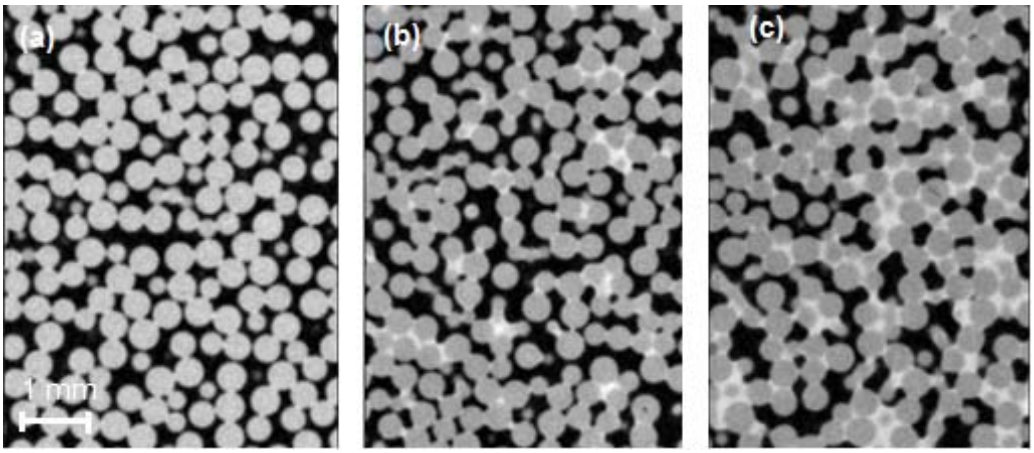

Figure 3: Horizontal slices through 3D tomographic images of randomly distributed polystyrene beads of 500 µm diameter at various liquid contents $\varepsilon = 0.015$ (a), $\varepsilon = 0.03$ (b), and $\varepsilon = 0.075$ (c). Liquid and air appear as white and black areas respectively, while the beads appear as gray discs. The slice cuts the beads at different heights and thus the beads appear to be more polydisperse than they actually are.

For a quantitative analysis of the tomographic images, the raw data had to be smoothed (to reduce the noise of the images) and segmented (to constitute entities that correspond for example to the solid, gaseous and liquid phases in the case of an unsaturated granular media). At each step, a wide range of existing tools can be used [63]. In the first pre-processing step, we reduce the noise in each image by applying a bilateral filter and then a "rolling ball" algorithm is used to correct for uneven illuminated background by simple thresholding method. The second step is the segmentation of images in which the grain and liquid phase were used respectively to extract the volume, the surface and the position of grains on one hand and the liquid content one on the other hand. All further analyses of the segmented images were performed with custom-made programs using *Python programming language*. In this way, we obtained the statistics of the number of capillary bridges and liquid clusters in contact with a bead, as well as the volume of individual liquid clusters.

In the X-ray microtomographic images, we can clearly distinguish liquid capillary bridges and liquid clusters by their morphologies. The capillary bridge is the liquid morphology between two particles and a 3D capillary bridge is shown in Figure 4. The limited resolution of the X-ray microtomography results in deviations from the real shape of the capillary bridges. For example capillary bridges with two particles in contact can be resolved as ‘donuts’ with a hole in the center and the diameter of this

hole will decrease as the voxel resolution is increased. In addition, a statistical analysis of the tomography data reveals that the number of capillary liquid bridges decreases as ε increases further since capillary bridges merge into liquid clusters. Indeed, it is found in Figure 5 that their frequency in the sample decreases from 85% at $\varepsilon =$ 0.03 to 24% at $\varepsilon =$ 0.075. Beside the capillary bridges, the trimer is the most frequent morphology at $\varepsilon =$ 0.03 with 12%. In contrast, trimers and other more complex morphologies become more common with 37% and 38% respectively for $\varepsilon =$ 0.075 than simple capillary bridges which represent only 25%.

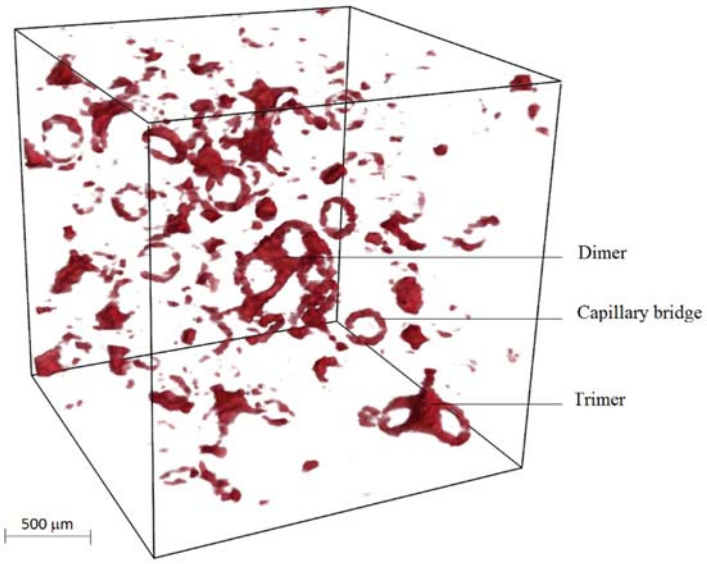

Figure 4: Shapes of some isolated liquid cluster morphologies. For a deep view, beads and air are hidden

The size of the percolating cluster grows as the liquid content is further increased [33]. The smallest liquid clusters are here referred to 'dimer' and 'trimer'. They are formed between three beads: the dimer has two contact points between the particles as shown in Fig. 4 and as depicted in the schematic inset in Fig. 5(a), while the trimer has three contact points (Fig. 4; Fig. 5(a)). Another larger cluster is illustrated in Fig. 5(b) – pentamer – cluster that has five contacts between four beads. Moreover, to explore how the number of capillary bridges and other morphologies on a bead varies with the shear strain, we prepared samples with a fixed liquid content: $\varepsilon =$ 0.03 and $\varepsilon =$ 0.075. The shear strain γ was varied between 0 and 35. Note that, since shear is inhomogeneous in a parallel plate geometry, we restrict the analysis of liquid morphology to the region of the gap of radial position $0.45R_p \le r \le 0.9R_p$. In this region, shear is roughly homogeneous, and the microstructure can be

studied as a function of the average shear strain $\gamma = \theta R_{mean} / h$ by changing the angular displacement θ of the upper plate of the geometry in which R_{mean} is defined as $R_{mean} = \left(0.45R_p + 0.9R_p\right)/2$.

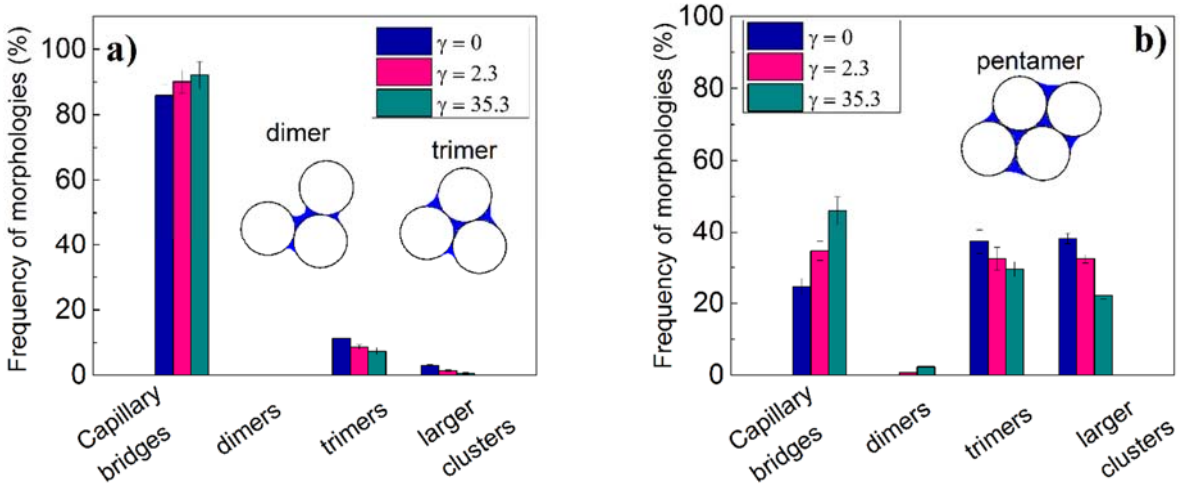

Figure 5: Histogram of the frequency of liquid cluster morphologies as a function of shear deformation for two liquid contents $\varepsilon = 0.03$ (a), and $\varepsilon = 0.075$ (b).

Since particles and also the wetting fluid must not move during the time of a scan , this leads us to apply to our sample a given shear strain, then stop the flow and image the material at rest with a "frozen" structure, which is supposed to be close to the structure under flow [51]. The underlying hypothesis is that relaxation of the microstructure at rest is negligible. However, when the shear is stopped, a certain time is needed for the liquid morphologies to equilibrate [33]. During this process, small capillary bridges will grow on the expense of larger clusters. A time series of tomographies was recorded 10 min after the shear has been stopped.

Figure 5 shows a histogram of the frequency of occurrence of liquid capillary bridges and other morphologies found in a granular pile with two liquid contents $\varepsilon = 0.03$ and $\varepsilon = 0.075$ for different values of shear deformation. A puzzling observation is that the total number of capillary bridges increases, at the expense of other morphologies, when we increase the shear strain. Due to the motion of grains, the liquid is redistributed to neighbouring contacts after a steady rupture of large clusters leading to a redistribution of liquid on large scales [42].

2. CONSTITUTIVE LAWS: EXPERIMENTS VERSUS DEM SIMULATIONS

Typical experimental measurements are shown in Fig. 6, where we start out with a gap h_0, which represents typically few particle diameters ($10d_p$ to $45d_p$), impose a constant $\dot{\gamma}$ and F_n and measure the torque T and the gap h as functions of strain (or time).

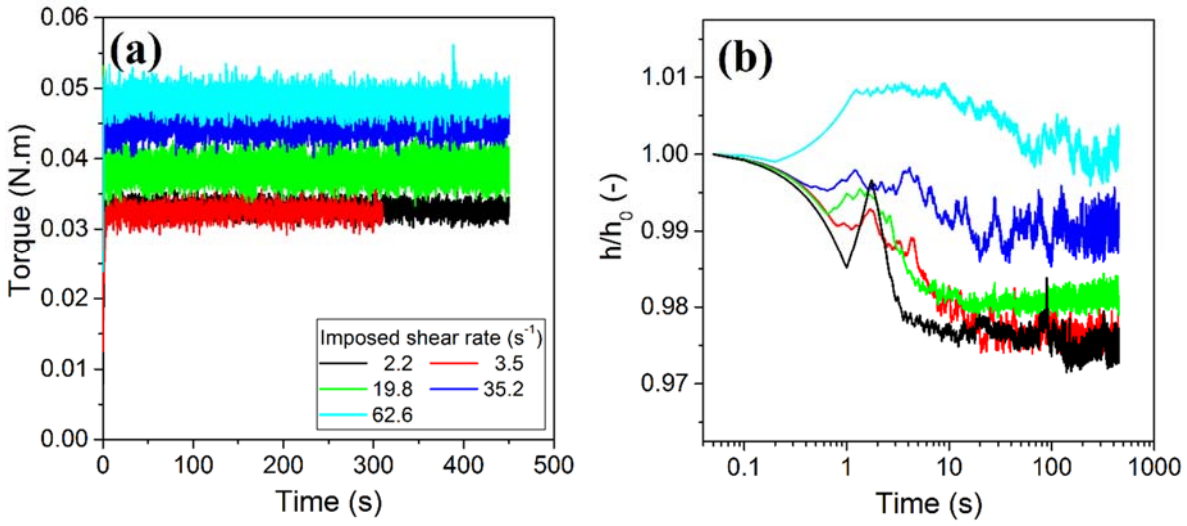

Figure 6: Evolution as a function of time at 2.96N imposed normal force under different applied shear rates of: (a) the driving torque and (b) the rescaled gap size. (Only few curves are shown for clarity)

The system reaches a steady state after a certain amount of strain: the critical state is defined by the local shear accumulated over time under a constant confining pressure and constant strain rate condition. This state is reached after a large enough strain, when the material deforms with applied shear without any change in state variables, independently of the initial condition. Note that dense materials show a systematic dilation while loose samples present a compaction before reaching their critical state [11].

Here we present general definitions of the averaged macroscopic quantities – including strain rate, stresses and the solid volume fraction. In the annular plate-cup shear geometry, the driving torque is related to the local value τ of the shear stress by:

$$T = 2\pi \int_{R_i}^{R_o} \tau r^2 dr \qquad \text{(Eq.4)}$$

where R_i = 21 mm and R_o = 45 mm are inner and outer radii of the annular trough. If the radial velocity gradient is neglected [64,65] into the annular trough, the shear stress is quasi-independent of the radial position *r* and thus, integrating Eq. (4) yields the shear stress as:

$$\tau = 3T / 2\pi \left(R_o^3 - R_i^3 \right) \quad \text{(Eq.5)}$$

Equation (5) holds because the lateral contribution of walls friction on the stress distribution within the granular sample can be neglected due to the lubrication from the wetting liquid [55]. Moreover, the cylinders of our annular shear cell, made of polyoxymethylene (POM) resin, were finished as smoothly as possible to permit the granular material to slip there as readily as possible [11].

The normal stress can also be calculated from the normal force as follows:

$$\sigma_n = \left(F_n + mg/2 \right) / \pi \left(R_o^2 - R_i^2 \right) \quad \text{(Eq.6)}$$

Note that for $h_0 \approx (10-45)\, d_p$, the imposed normal stress is larger than the hydrostatic pressure once F_n is larger than 1.20 N, meaning that gravity may be neglected for the explored range of imposed normal forces.

Besides, assuming that the velocity gradient is approximately uniform over the depth and width of the annular trough and a no-slip condition exists at the rough upper and lower shearing walls, one can estimate the mean shear rate averaged across the annulus as:

$$\dot{\gamma} = \Omega \left(R_o + R_i \right) / 2h \quad \text{(Eq.7)}$$

And the mean shear strain is given by:

$$\gamma = \theta \left(R_o + R_i \right) / 2h \quad \text{(Eq.8)}$$

where θ and Ω are respectively the angular displacement and the rotation speed of the upper plate.

The spaces between the moving upper plate and the side vertical walls are smaller than 100 μm, which is five times as small as the grain size. Since these gaps are so narrow that grains cannot escape from the shear cell, one can measure unambiguously the solid fraction from the gap variation and the mass m of grains as:

$$\phi_S = m / \pi \rho_p h \left(R_o^2 - R_i^2 \right) \quad \text{(Eq.9)}$$

where m is the total mass of the wet granular material.

The vertical position $h(t)$ of the plate indicates the dilation or compaction of the granular material.

We define the macroscopic friction coefficient of the unsaturated granular material is set equal to the time average – in the steady state – of the ratio of the shear stress τ to the confining pressure σ_n $\mu_w^* = \tau / \sigma_n$. The macroscopic rheological response of the system of wet particles can therefore be expressed as the non-dimensional macroscopic friction coefficient μ_w^* and solid fraction variations ϕ_S versus the inertial number I for various P^*. For both quantities, a good agreement between experiments and simulations is observed without any adjustable parameter once the intergranular friction coefficient is set to its appropriate value [3].

Figure 7(a) shows, for different values of P^*, how μ_w^* varies throughout the flow regimes. Here μ_w^* approaches a finite nonzero value in the quasistatic limit ($I \leq$ 0.001) which is strongly influenced by capillary forces: it increases with decreasing P^*. When the inertial number is increased, μ_w^* increases whatever the reduced pressure. Moreover, all data points are above the curve of the cohesionless dry beads (in the absence of the capillary forces: $P^* \to \infty$): $\mu_w^*(I, P^*)$ is a decreasing function of P^*, whatever the value of I.

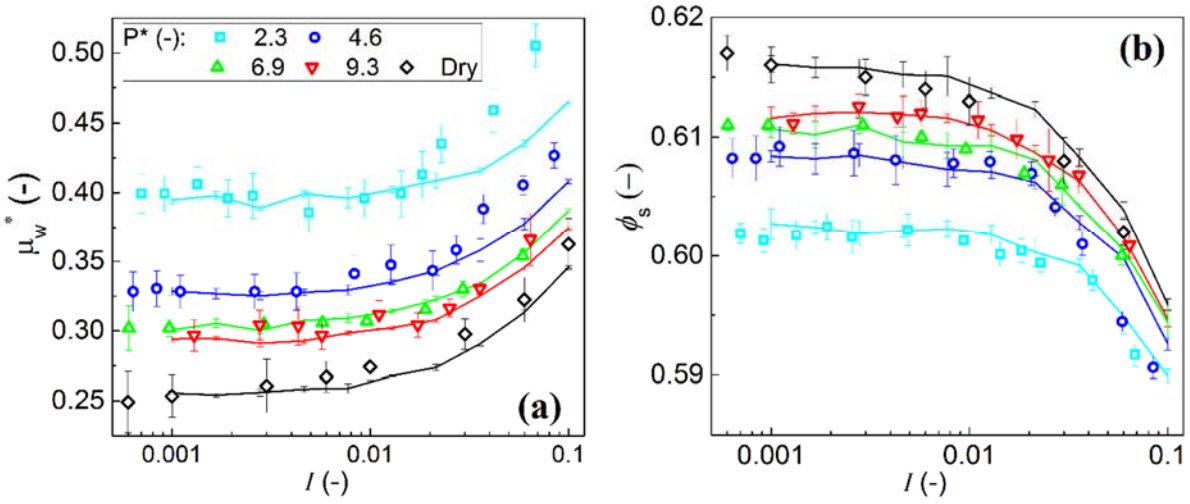

Figure 7: Experimental (symbols) and simulation (lines) results for macroscopic friction coefficient μ_w^* (a) and solid fraction ϕ_S (b) versus inertial number I for different values of reduced pressure P^*. The error bars correspond to the standard deviation of the torque and the gap level in the steady state.

Complementary information is the *dynamical dilatancy law*, which describes the variations of the solid fraction as a function of the inertial number: ϕ_S decreases with increasing I (Fig. 7(b)). As for the friction coefficient, the solid fraction variation is strongly influenced by P^*: ϕ_S is an increasing function of P^* for the explored range of inertia number. In the quasistatic regime, the solid fraction decreases from 0.615 to 0.605 when P^* decreases.

The increase of μ_w^* and the decrease of ϕ_S for moderate values of I show the usual behavior of granular materials under shear flow, similar to other studies on dry grains reported in the experimental and numerical literature [2,7,10–12,29]. The shear resistance appears however, to be underestimated by the simulations: μ_w^* grows faster with I in the experiments than in simulations. However, the transition between the quasistatic and intermediate regimes tends to occur at small I as P^* increases so that the friction coefficient (respectively, the solid fraction) increases (decreases) faster for the dry sample than for the wet ones. Indeed, as contacts are stabilized by attractive (capillary) forces that hold the granular system together, they do not so easily open when the network is being sheared that should limit the dilating tendency of faster flows [15].

For wet granular materials, however, to establish constitutive laws of the flow, it is essential to ensure that the flow, at least from a macroscopic point of view, is homogeneous. Only a few published studies investigated the effects of cohesion on shear banding: [66] concerning dense adhesive emulsions, [67] on cemented granular media and [2,68] on wet granular media. Rheological studies on adhesive and nonadhesive emulsions [66,69] reported that the presence of attractive forces at contact affects shear banding by affecting flow heterogeneity and wall slip. In wet granular materials, Khamseh and co-workers have shown from DEM simulations a permanent shear banding for low $P^* = 0.1$ and that the localization tendency of the flow increases for smaller values of inertial number. To investigate that effect, we have varied the initial size of the gap from $10d_p$ to $44d_p$.

Figure 8 illustrates the evolution of the friction coefficient and of the solid fraction with the gap heights for P^* = 2.3 and $I = 0.03$: it shows that changing the gap does not significantly affect these results. This suggests a total absence of shear localization at this reduced pressure. However, at small $P^* \leq 2$, the resolution of our measurements is not sufficient to dismiss the possibility that shear localization arises. This is why the explored P^* values are restricted to the range of $P^* \geq 2$.

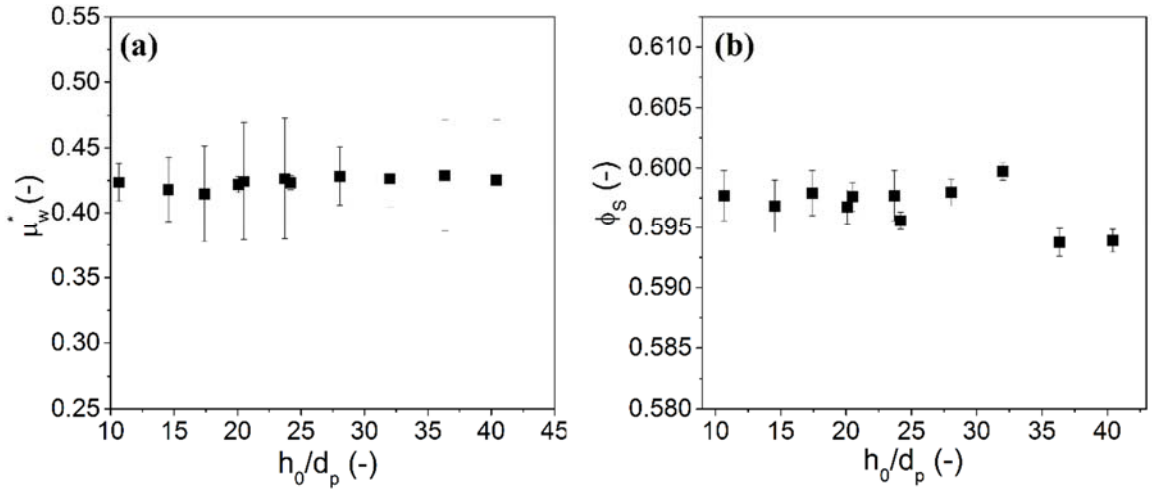

406

407 Figure 8: Macroscopic friction coefficient and solid fraction versus gap at I =0.03 and P^* = 2.3.

408

409 3. MACROSCOPIC COHESION

410 Previously reported experiments of unsaturated granular materials show that the tensile strength and
411 the yield stress have a typical dependence on the wetting liquid fraction [70]. The friction coefficient
412 μ_w^* in the quasistatic regime increases with decreasing P^* and increasing the liquid content [3]. If
413 there is no geometric ordering of the system, it has been argued that these capillary forces introduce
414 a predominantly isotropic compressive stress into the system [16]. The effective stress of the wet
415 granular material will then be in each case represented by a Mohr circle shifted to the right with both
416 principal stresses increased by the value of the isotropic compressive stress. In the case of non-
417 cohesive dry materials, the steady shear stress is a linear function of pressure, as predicted by the
418 Mohr-Coulomb criterion with a slope that increases with increasing shear rate [11]. However, for wet
419 granular materials, the relation between shear stress and confining pressure becomes non-linear when
420 cohesion c is introduced at the contacts due to capillary forces. Taking c independent of P^*, (Eq. 1)
421 implies that the friction coefficient μ_w^* should vary linearly with $1/P^*$ as:

422 $$\mu_w^* = \mu_d^* + \frac{C^*}{P^*} \qquad \text{(Eq.10)}$$

423 where $C^* = cd_p / \pi\Gamma$ is a dimensionless cohesion and μ_d^* the friction coefficient of the dry sample.

To evidence that, measurements were done in the quasistatic regime with samples subjected to a very low shear rate under different confining pressures corresponding to an inertia number of I = 0.001. The resulting steady stresses and solid fraction were measured in the same way as discussed above. Figure 9(a) uses Eq. 10 to identify values of cohesion C^*. Indeed, the linearity of the graphs shows that the Mohr-Coulomb criterion fits well the experimental points, at least as long as $P^* \geq 2$. For smaller P^*, the shear resistance is overestimated by the Mohr-Coulomb criterion. Moreover, we evidence once again that when $P^* \to \infty$, wet granular material behaves as a dry one and the friction coefficient goes to $\mu_w^* \approx \mu_d^* = 0.25$ that coincides with the internal friction coefficient of the material in its critical state. (Fig. 7a).

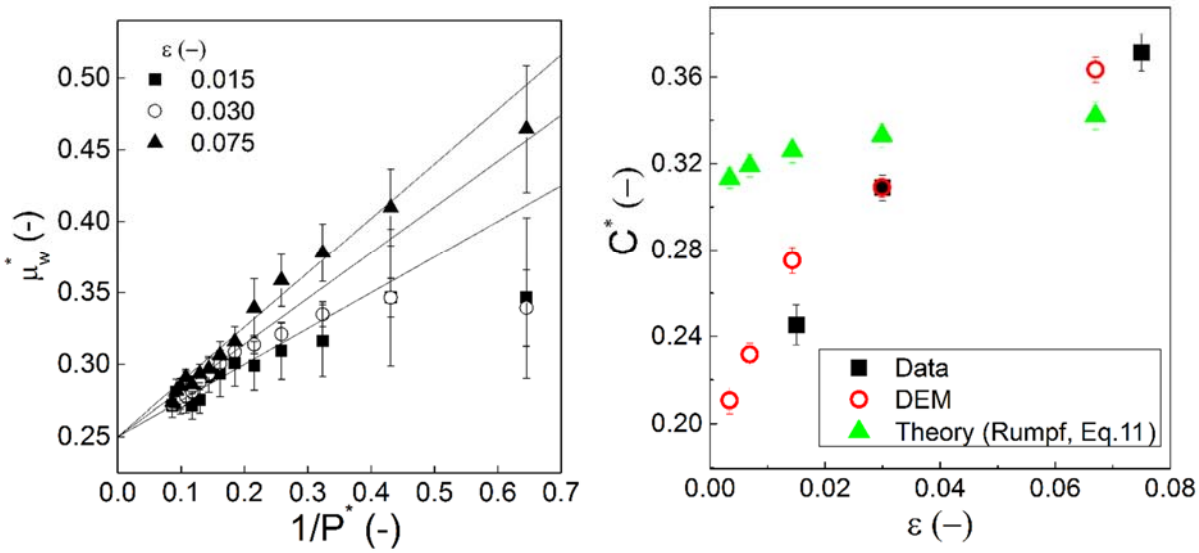

Figure 9: (a) Linear increase of μ_w^* with $1/P^*$ for different liquid content. (b) Dimensionless cohesion versus liquid content, as measured in experiments and DEM simulations, and as predited by the Rumpf expression in (Eq. 11).

Figure 9(b) shows that the macroscopic cohesion C^*, which is the slope of the linear increase of μ_w^* vs. $1/P^*$, is a growing function of the liquid content. Furthermore, a fair agreement between experiments and numerical simulations is found. More complete numerical results are presented in [3], in which a detailed numerical study of the influence of the parameters (intergranular friction coefficient μ, liquid content ε) on this cohesion, on the hypothesis of the quasistatic effective stresses, and the relations of the shear resistance with different variables characterizing the state of

444 the material (coordination, orientations of the bridges liquids ...) are considered. This result is
445 consistent with the cohesion in static shear strength experiments conducted on glass beads by
446 Richefeu et al. [37] and the relation between the cohesion and the liquid content seems to follow a
447 similar trend as that for the elastic modulus with the liquid content [45,70]. In the *pendular* regime,
448 the macroscopic cohesion increases with the increasing liquid bridge volume [38,59].

449 We now discuss a possible estimation way to predict the *friction law* of wet granular material applying
450 the Rumpf model [71]. In the quasistatic regime, according to Rumpf's theory, values of cohesion C^*
451 of wet granular materials in the *pendular* regime could be estimated with the following expression
452 [2,35,37]:

453 $$C^* = \mu_d^* \frac{Z\phi_S}{\pi} \qquad \text{(Eq.11)}$$

454 where Z is the liquid bridge coordination number, ϕ_S and μ_d^* are respectively the experimental data,
455 in the quasistatic regime, of the solid fraction of the wet sample and the friction coefficient of the dry
456 material.

457 In the quasistatic regime, Eq. 11 correctly predicts the macroscopic dimensionless cohesion for the
458 higher liquid contents in the investigated range (Fig. 9b), but overestimates it at lower liquid contents,
459 for which it fails to capture the decreasing trend.

460 Furthermore, taking thus the coordination number roughly constant of I and P^* (Khamseh et al.
461 2015), Eq. 1 implies that the theoretical friction coefficient $\mu_{w\_th}^*$ can be written as:

462 $$\mu_{w\_th}^*\left(I,P^*\right) = \mu_d^*\left(I\right)\left[1+\frac{Z\phi_S\left(I,P^*\right)}{\pi P^*}\right] \qquad \text{(Eq.12)}$$

463 From the experimental measurements of the friction coefficient of dry grains and of the solid fraction
464 of the wet sample for a given reduced pressure (Fig. 7), Figure 10 shows that (Eq. 12) provides a good
465 estimation of the friction coefficient of the unsaturated wet granular material for different liquid
466 content. Note that some constant value of the wet coordination number $Z = 6.2$ has to be chosen in
467 (Eq. 12). This high liquid bridge coordination number can be explained by the higher bridge
468 connectivity in close packings: values close to 6 and 6.5 for respectively a loose and dense packings
469 were observed from [72] in experiments and between 6.8 and 4.8 in simulations [2]. Note that
470 however, this liquid bridge coordination number can be obtained from the X-ray microtomography
471 images but further analysis is required.

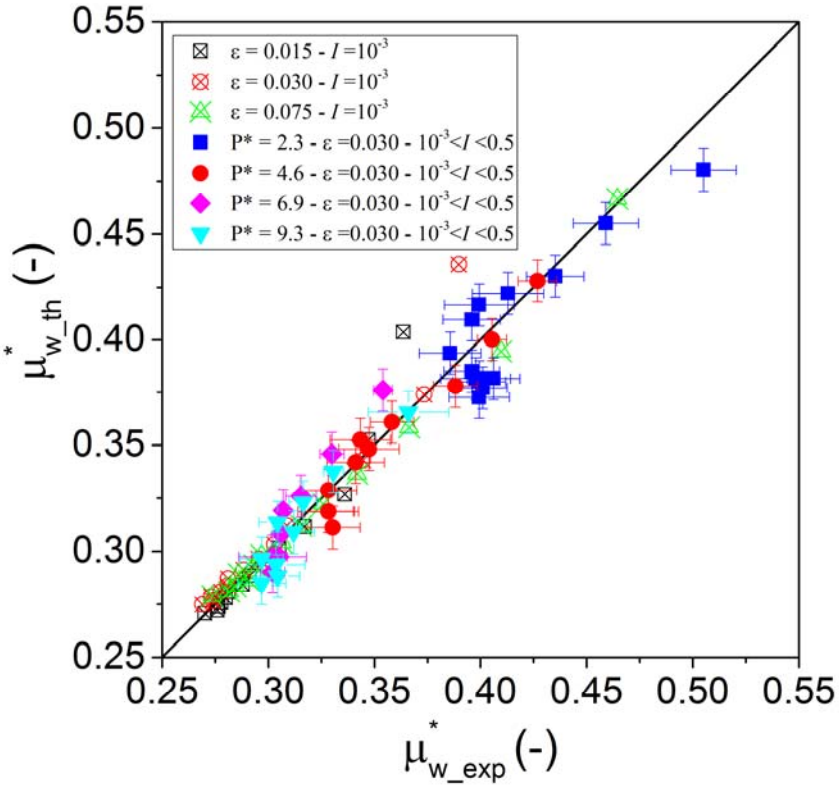

Figure 10: Predicted values of the friction coefficient using Eq. 11 versus the measured ones, in the quasistatic and inertial flow regimes and for all liquid contents.

IV. CONCLUSION

This paper examines experimentally the transition from the yielding to the flowing behavior of unsaturated wet granular materials. Attention was focused on homogeneously sheared assemblies of particles in an annular shear cell. From well controlled rheometric measurements (under imposed confining normal stress and applied shear rate) and using two simple characterization tools (the inertial number and the reduced pressure), the internal state of wet granular materials is described. Summarizing, we find that there is a pronounced effect of the addition of small amounts of wetting liquid to dry granular matter. It is observed that the conventional $\mu(I)-$ rheology (usually used for dry granular matter) must be modified to take into account other factors such as cohesion as already observed from DEM simulations [2,29]. Compared to dry granular materials, the wet ones exhibit a similar behavior, however, which is dependent on the reduced pressure P^*. While the macroscopic friction coefficient increases when P^* decreases, the solid volume fraction is a decreasing function of

489 P^*. Such a strong influence of cohesive forces contrasts with the 2D numerical results of [29,32], in
490 which similar deviations between cohesionless and cohesive systems are not observed until P^*
491 decreases to much lower values, of order 0.3.

492 Additionally, in the quasistatic regime, a simple effective stress approach may quantitatively account
493 for the shear resistance trend in good approximation as long as $P^* \geq 2$. The Mohr- Coulomb criterion
494 approximately describes critical states in the same reduced pressure range, but is no longer applicable
495 at lower P^*. Also results of DEM simulations are shown to agree quantitatively with experimental
496 ones, provided the right value $\mu \approx 0.09$ is given to the intergranular friction coefficient, as identified
497 from the macroscopic properties of the dry material. Once the value of $\mu \approx 0.09$ is determined from
498 the dry case (to calibrate the simulations), there is indeed no more adjustable parameter for the wet
499 sample. Note however, one limitation of the DEM model is its inability to deal with liquid contents
500 exceeding the pendular regime. Numerical models for higher liquid contents, resorting, e.g., to a lattice
501 Boltzmann discretization of the interstitial liquid, are currently being developed [73–75].

502 Further use of X-ray tomography technique enabled investigations of the microstructure. It is found
503 that, for the explored range of liquid content, samples stay homogeneous with however the presence
504 of a multitude complex morphologies far from simple capillary bridges. We also observed that shearing
505 tends to reduce the number of these large liquid morphologies to the cost of simple liquid bridges.
506 This important result seems to explain the concordance between experimental and numerical
507 measurements. Indeed, the numerical model is restricted to the *pendular state*, in which the liquid
508 phase is completely discontinuous and no coalescence occurs between liquid bridges.

509 We believe that the experimental techniques described in this work can be successfully used as a
510 means of investigating the properties of wet cohesive granular materials flows. But as we consider
511 dynamics, there must also be viscous interactions between moving grains, and even the liquid inertia
512 must become important for fast dynamics [41,42]. Indeed, the liquid content and the hysteresis for
513 liquid bridge creation and rupture between approaching or receding grain pairs have been observed
514 to significantly affect the rheology in simulations [2]. Unfortunately, such dynamical effects have been
515 difficult to characterize with conventional rheometric techniques. However, in an ongoing project, we
516 plan to image the evolution of the microstructure under shear with a shear device inserted into MRI
517 imager, enabling local measurements of granular solid fraction and liquid content. A direct access to
518 the velocity or strain field was shown to be crucial to a correct measurement of rheological laws for
519 materials in which strains tend to localize in shear zones [76].

520

ACKNOWLEDGMENTS

We thank D. Hautemayou and C. Mézière for technical helps for the measurements. We gratefully acknowledge financial support from the Agence Nationale de la Recherche (Grant No. ANR-16-CE08-0005-01). The Laboratoire Navier microtomograph has been acquired with the financial support of Region Ile-de-France (SESAME program) and F2M (Fédération Française de Mécanique).

REFERENCES

[1] B. Andreotti, Y. Forterre, O. Pouliquen, Granular Media; Between Fluid and Solid, Cambridge Univ. Press. 55 (2013) ISBN-13: 978-1107034792. doi:10.1080/00107514.2014.885579.

[2] S. Khamseh, J.N. Roux, F. Chevoir, Flow of wet granular materials: A numerical study, Phys. Rev. E. 92 (2015) 022201. doi:10.1103/PhysRevE.92.022201.

[3] M. Badetti, A. Fall, F. Chevoir, J.-N. Roux, Shear strength of wet granular materials: macroscopic cohesion and effective stress, Eur. Phys. J. E. 41 (2018). doi:10.1140/epje/i2018-11677-8.

[4] N. Mitarai, F. Nori, Wet granular materials, Adv. Phys. 55 (2006) 1–45. doi:DOI 10.1080/00018730600626065.

[5] S.M. Iveson, J.D. Litster, K. Hapgood, B.J. Ennis, Nucleation, growth and breakage phenomena in agitated wet granulation processes: A review, Powder Technol. 117 (2001) 3–39. doi:10.1016/S0032-5910(01)00313-8.

[6] S. Herminghaus, Dynamics of wet granular matter, Adv. Phys. 54 (2005) 221–261. doi:10.1080/00018730500167855.

[7] GDR Midi, On dense granular flows., Eur. Phys. J. E. Soft Matter. 14 (2004) 341–65. doi:10.1140/epje/i2003-10153-0.

[8] M. Pakpour, M. Habibi, P. Møller, D. Bonn, How to construct the perfect sandcastle, Sci. Rep. 2 (2012). doi:10.1038/srep00549.

[9] F. Da Cruz, S. Emam, M. Prochnow, J.N. Roux, F. Chevoir, Rheophysics of dense granular materials: Discrete simulation of plane shear flows, Phys. Rev. E. 72 (2005) 021309. doi:10.1103/PhysRevE.72.021309.

549 [10] P. Jop, Y. Forterre, O. Pouliquen, A constitutive law for dense granular flows., Nature. 441
550 (2006) 727–730. doi:10.1038/nature04801.

551 [11] A. Fall, G. Ovarlez, D. Hautemayou, C. Mézière, J.-N. Roux, F. Chevoir, Dry granular flows :
552 Rheological measurements of the μ (I) -rheology, J. Rheol. (N. Y. N. Y). 59 (2015) 1065–1080.
553 doi:10.1122/1.4922653.

554 [12] T. Hatano, Power-law friction in closely packed granular materials, Phys. Rev. E. 75 (2007) 1–4.
555 doi:10.1103/PhysRevE.75.060301.

556 [13] L. Staron, P.Y. Lagrée, C. Josserand, D. Lhuillier, Flow and jamming of a two-dimensional
557 granular bed: Toward a nonlocal rheology?, Phys. Fluids. 22 (2010) 1–10.
558 doi:10.1063/1.3499353.

559 [14] J.. M.N.T. Gray, A.N. Edwards, A depth-averaged μ(I)-rheology for shallow granular free-
560 surface flows, J. Fluid Mech. 755 (2014) 503–534. doi:10.1017/jfm.2014.450.

561 [15] J.E. Fiscina, M. Pakpour, A. Fall, N. Vandewalle, C. Wagner, D. Bonn, Dissipation in
562 quasistatically sheared wet and dry sand under confinement, Phys. Rev. E. 86 (2012) 020103.
563 doi:10.1103/PhysRevE.86.020103.

564 [16] P. Pierrat, D.K. Agrawal, H.S. Caram, Effect of moisture on the yield locus of granular
565 materials: Theory of shift, Powder Technol. 99 (1998) 220–227. doi:10.1016/S0032-
566 5910(98)00111-9.

567 [17] L. Bocquet, E. Charlaix, S. Ciliberto, J. Crassous, Moisture-induced ageing in granular media
568 and the kinetics of capillary condensation, Nature. 396 (1998) 735–737. doi:10.1038/25492.

569 [18] L. Bocquet, É. Charlaix, F. Restagno, Physics of humid granular media, Comptes Rendus Phys. 3
570 (2002) 207–215. doi:10.1016/S1631-0705(02)01312-9.

571 [19] P. Tegzes, T. Vicsek, P. Schiffer, Development of correlations in the dynamics of wet granular
572 avalanches, Phys. Rev. E. 67 (2003) 051303. doi:10.1103/PhysRevE.67.051303.

573 [20] S.T. Nase, W.L. Vargas, A.A. Abatan, J.J. McCarthy, Discrete characterization tools for cohesive
574 granular material, Powder Technol. 116 (2001) 214–223. doi:10.1016/S0032-5910(00)00398-
575 3.

576 [21] L. Chun-Chung, H. Shu-San, Experimental analysis of the dynamic properties of wet granular
577 matter, Powder Technol. 197 (2010) 222–229. doi:10.1016/j.powtec.2011.09.010.

578 [22] A. Samadani, A. Kudrolli, Segregation transitions in wet granular matter, (2000) 2–5.
579 doi:10.1103/PhysRevLett.85.5102.

580 [23] A. Samadani, A. Kudrolli, Angle of repose and segregation in cohesive granular matter, Phys.
581 Rev. E. 64 (2001) 051301. doi:10.1103/PhysRevE.64.051301.

582 [24] M. Scheel, D. Geromichalos, S. Herminghaus, Wet granular matter under vertical agitation, J.
583 Phys. Condens. Matter. 16 (2004) S4213–S4218. doi:10.1088/0953-8984/16/38/033.

584 [25] P.R. Day, G.G. Holmgren, Microscopic Changes in Soil Structure During Compression1, Soil Sci.
585 Soc. Am. J. 16 (1952) 73–77. doi:10.2136/sssaj1952.03615995001600010022x.

586 [26] D. Geromichalos, M.M. Kohonen, F. Mugele, S. Herminghaus, Mixing and Condensation in a
587 Wet Granular Medium, Phys. Rev. Lett. 90 (2003) 168702.
588 doi:10.1103/PhysRevLett.90.168702.

589 [27] T.A. Ghezzehei, D. Or, Dynamics of soil aggregate coalescence and theological processes,
590 Water Resour. Res. 36 (2000) 367–379.

591 [28] N. Mitarai, Granular flow: dry and wet, Eur. Phys. J. Spec. Top. 204 (2012) 5–17.

592 [29] N. Berger, E. Azéma, J.-F. Douce, F. Radjai, Scaling behaviour of cohesive granular flows,
593 Europhys. Lett. 112 (2015) 64004. doi:10.1209/0295-5075/112/64004.

594 [30] V.-D. Than, S. Khamseh, A.M. Tang, J. Pereira, F. Chevoir, J.-N. Roux, Basic Mechanical
595 Properties of Wet Granular Materials : A DEM Study, J. Eng. Mech. 143 (2017) C4016001.
596 doi:10.1061/(ASCE)EM.1943-7889.0001043.

597 [31] P.G. Rognon, J.-N. Roux, D. Wolf, M. Naaïm, F. Chevoir, Rheophysics of cohesive granular
598 materials, Europhys. Lett. 74 (2006) 644. doi:10.1209/epl/i2005-10578-y.

599 [32] P.G. Rognon, J.-N. Roux, M. Naaïm, F. Chevoir, Dense flows of cohesive granular materials ¨, J.
600 Fluid Mech. 596 (2008) 21–47. doi:10.1017/S0022112007009329.

601 [33] M. Scheel, R. Seemann, M. Brinkmann, M. Di Michiel, A. Sheppard, B. Breidenbach, S.
602 Herminghaus, Morphological clues to wet granular pile stability., Nat. Mater. 7 (2008) 189–
603 193. doi:10.1038/nmat2117.

604 [34] T. Mikami, H. Kamiya, M. Horio, Numerical simulation of cohesive powder behavior in a
605 fluidized bed, Chem. Eng. Sci. 53 (1998) 1927–1940. doi:10.1016/S0009-2509(97)00325-4.

606 [35] T. Gröger, U. Tüzün, D.M. Heyes, Modelling and measuring of cohesion in wet granular
607 materials, Powder Technol. 133 (2003) 203–215. doi:10.1016/S0032-5910(03)00093-7.

608 [36] L. Scholtès, B. Chareyre, F. Nicot, F. Darve, Micromechanics of granular materials with
609 capillary effects (DOI:10.1016/j.ijengsci.2008.07.002), Int. J. Eng. Sci. 47 (2009) 1460–1471.
610 doi:10.1016/j.ijengsci.2009.10.003.

611 [37] V. Richefeu, M.S. El Youssoufi, F. Radjaï, Shear strength properties of wet granular materials,
612 Phys. Rev. E. 73 (2006) 1–11. doi:10.1103/PhysRevE.73.051304.

613 [38] X. Chateau, P. Moucheront, O. Pitois, Micromechanics of Unsaturated Granular Media, J. Eng.
614 Mech. 128 (2002) 856–863. doi:10.1061/(ASCE)0733-9399(2002)128:8(856).

615 [39] F. Soulié, M.S. El Youssoufi, F. Cherblanc, C. Saix, Capillary cohesion and mechanical strength
616 of polydisperse granular materials, Eur. Phys. J. E. 21 (2006) 349–357.
617 doi:10.1140/epje/i2006-10076-2.

618 [40] F.A. Gilabert, J.N. Roux, A. Castellanos, Computer simulation of model cohesive powders:
619 Plastic consolidation, structural changes, and elasticity under isotropic loads, Phys. Rev. E. 78
620 (2008) 031305. doi:10.1103/PhysRevE.78.031305.

621 [41] R. Mani, D. Kadau, H.J. Herrmann, Liquid migration in sheared unsaturated granular media,
622 Granul. Matter. 15 (2013) 447–454. doi:10.1007/s10035-012-0387-3.

623 [42] R. Mani, D. Kadau, D. Or, H.J. Herrmann, Fluid depletion in shear bands, Phys. Rev. Lett. 109
624 (2012) 1–5. doi:10.1103/PhysRevLett.109.248001.

625 [43] V. Richefeu, M.S. El Youssoufi, F. Radjaï, Shear strength properties of wet granular materials,
626 Phys. Rev. E. 73 (2006) 1–11. doi:10.1103/PhysRevE.73.051304.

627 [44] G. Lefebvre, P. Jop, Erosion dynamics of a wet granular medium, Phys. Rev. E. 88 (2013).
628 doi:10.1103/PhysRevE.88.032205.

629 [45] A. Fall, B. Weber, M. Pakpour, N. Lenoir, N. Shahidzadeh, J.E. Fiscina, C. Wagner, D. Bonn,
630 Sliding friction on wet and dry sand, Phys. Rev. Lett. 112 (2014) 3–6.
631 doi:10.1103/PhysRevLett.112.175502.

632 [46] G. Saingier, A. Sauret, P. Jop, Accretion Dynamics on Wet Granular Materials, Phys. Rev. Lett.
633 118 (2017). doi:10.1103/PhysRevLett.118.208001.

634 [47] W.L. Yang, S.S. Hsiau, Wet granular materials in sheared flows, Chem. Eng. Sci. 60 (2005)

635 4265–4274. doi:10.1016/j.ces.2005.03.001.

636 [48] W.L. Yang, S.S. Hsiau, The effect of liquid viscosity on sheared granular flows, Chem. Eng. Sci.
637 61 (2006) 6085–6095. doi:10.1016/j.ces.2006.05.033.

638 [49] C. Semprebon, M. Scheel, S. Herminghaus, R. Seemann, M. Brinkmann, Liquid morphologies
639 and capillary forces between three spherical beads, Phys. Rev. E. 94 (2016) 012907.
640 doi:10.1103/PhysRevE.94.012907.

641 [50] J.F. Bruchon, J.M. Pereira, M. Vandamme, N. Lenoir, P. Delage, M. Bornert, Full 3D
642 investigation and characterisation of capillary collapse of a loose unsaturated sand using X-ray
643 CT, Granul. Matter. 15 (2013) 783–800. doi:10.1007/s10035-013-0452-6.

644 [51] G. Ovarlez, F. Mahaut, S. Deboeuf, N. Lenoir, S. Hormozi, X. Chateau, Flows of suspensions of
645 particles in yield stress fluids, J. Rheol. (N. Y. N. Y). 59 (2015) 1449–1486.
646 doi:10.1122/1.4934363.

647 [52] S. Deboeuf, N. Lenoir, D. Hautemayou, M. Bornert, F. Blanc, G. Ovarlez, Imaging non-Brownian
648 particle suspensions with X-ray tomography: Application to the microstructure of Newtonian
649 and viscoplastic suspensions, J. Rheol. (N. Y. N. Y). 62 (2018) 643–663. doi:10.1122/1.4994081.

650 [53] M. Gholami, N. Lenoir, D. Hautemayou, G. Ovarlez, S. Hormozi, Time-resolved 2D
651 concentration maps in flowing suspensions using X-ray, Researchgate. (2017).
652 doi:10.13140/RG.2.2.15950.77129.

653 [54] S.B. Savage, M. Sayed, Stresses developed by dry cohesionless granular materials sheared in
654 an annular shear cell, J. Fluid Mech. 142 (1984) 391–430.
655 doi:10.1017/CBO9781107415324.004.

656 [55] F. Boyer, É. Guazzelli, O. Pouliquen, Unifying suspension and granular rheology, Phys. Rev.
657 Lett. 107 (2011) 1–5. doi:10.1103/PhysRevLett.107.188301.

658 [56] O. Kuwano, R. Ando, T. Hatano, Crossover from negative to positive shear rate dependence in
659 granular friction, Geophys. Res. Lett. 40 (2013) 1295–1299. doi:10.1002/grl.50311.

660 [57] A. Lemaître, J.N. Roux, F. Chevoir, What do dry granular flows tell us about dense non-
661 Brownian suspension rheology?, in: Rheol. Acta, 2009: pp. 925–942. doi:10.1007/s00397-009-
662 0379-3.

663 [58] G. Lian, C. Thornton, M.J. Adams, A theoretical study of the liquid bridge forces between two

rigid spherical bodies, J. Colloid Interface Sci. 161 (1993) 138–147. doi:10.1006/jcis.1993.1452.

[59] O. Pitois, P. Moucheront, X. Chateau, Liquid bridge between two moving spheres: An experimental study of viscosity effects, J. Colloid Interface Sci. 231 (2000) 26–31. doi:10.1006/jcis.2000.7096.

[60] C.D. Willett, M.J. Adams, S.A. Johnson, J.P.K. Seville, Capillary bridges between two spherical bodies, Langmuir. 16 (2000) 9396–9405. doi:10.1021/la000657y.

[61] D. Maugis, Adhesion of elastomers: Fracture mechanics aspects, J Adhes. Sci Tec. 1 (1987) 105. doi:10.1163/156856187X00120.

[62] P.S. Raux, A.L. Biance, Cohesion and agglomeration of wet powders, Phys. Rev. Fluids. 3 (2018). doi:10.1103/PhysRevFluids.3.014301.

[63] M. Coster, J.-L. Chermant, Image analysis and mathematical morphology for civil engineering materials, Cem. Concr. Compos. 23 (2001) 133–151. doi:10.1016/S0958-9465(00)00058-5.

[64] C. Coste, Shearing of a confined granular layer: Tangential stress and dilatancy, Phys. Rev. E. 70 (2004) 1–11. doi:10.1103/PhysRevE.70.051302.

[65] J.A.S. Cleaver, R.M. Nedderman, R.B. Thorpe, Accounting for granular material dilation during the operation of an annular shear cell, Adv. Powder Technol. 11 (2000) 385–399. doi:https://doi.org/10.1163/156855200750172015.

[66] A. Fall, J. Paredes, D. Bonn, Yielding and shear banding in soft glassy materials, Phys. Rev. Lett. 105 (2010). doi:10.1103/PhysRevLett.105.225502.

[67] N. Estrada, A. Lizcano, A. Taboada, Simulation of cemented granular materials. I. Macroscopic stress-strain response and strain localization, Phys. Rev. E. 82 (2010). doi:10.1103/PhysRevE.82.011303.

[68] R. Schwarze, A. Gladkyy, F. Uhlig, S. Luding, Rheology of weakly wetted granular materials: A comparison of experimental and numerical data, Granul. Matter. 15 (2013) 455–465. doi:10.1007/s10035-013-0430-z.

[69] J. Paredes, N. Shahidzadeh-Bonn, D. Bonn, Shear banding in thixotropic and normal emulsions, J. Phys. Condens. Matter. 23 (2011) 284116. doi:10.1088/0953-8984/23/28/284116.

693 [70] P.C.F. Møller, D. Bonn, The shear modulus of wet granular matter, Europhys. Lett. 80 (2007)
694 38002. doi:10.1209/0295-5075/80/38002.

695 [71] W. Pietsch, E. Hoffman, H. Rumpf, Tensile strength of moist agglomerates, Ind. Eng. Chem.
696 Prod. Res. Dev. 8 (1969) 58–62. doi:10.1021/i360029a009.

697 [72] M.M. Kohonen, D. Geromichalos, M. Scheel, C. Schier, S. Herminghaus, On capillary bridges in
698 wet granular materials, in: Phys. A Stat. Mech. Its Appl., 2004: pp. 7–15.
699 doi:10.1016/j.physa.2004.03.047.

700 [73] V. Richefeu, F. Radjai, J.Y. Delenne, Lattice Boltzmann modelling of liquid distribution in
701 unsaturated granular media, Comput. Geotech. 80 (2016) 353–359.
702 doi:10.1016/j.compgeo.2016.02.017.

703 [74] J.-N. Roux, A numerical toolkit to understand the mechanics of partially saturated granular
704 materials, J. Fluid Mech. 770 (2015) 1–4. doi:10.1017/jfm.2015.66.

705 [75] J.Y. Delenne, V. Richefeu, F. Radjai, Liquid clustering and capillary pressure in granular media,
706 J. Fluid Mech. 762 (2014). doi:10.1017/jfm.2014.676.

707 [76] A. Fall, F. Bertrand, D. Hautemayou, C. Mezière, P. Moucheront, A. Lemaître, G. Ovarlez,
708 Macroscopic discontinuous shear thickening versus local shear jamming in cornstarch, Phys.
709 Rev. Lett. 114 (2015) 1–5. doi:10.1103/PhysRevLett.114.098301.

710